Effects of Thermal Annealing on the Li^+ Intercalation Properties of $V_2O_5 \cdot nH_2O$ Xerogel Films

Ying Wang, Huamei Shang, Tammy Chou, and Guozhong Cao*

Materials Science and Engineering, University of Washington, 302 Roberts Hall, Box 352120, Seattle, Washington 98195

Received: March 11, 2005; In Final Form: April 16, 2005

$V_2O_5 \cdot nH_2O$ xerogel films with $n = 1.6$, 0.6, and 0.3 have been prepared from the sol−gel route by reacting V_2O_5 with H_2O_2 followed by drying under ambient conditions and thermal annealing at 110 and 250 °C, respectively. After dehydration, V_2O_5 crystallizes at 300−330 °C, as revealed by thermal gravimetric analysis and X-ray diffraction. Electrochemical characterization demonstrated that $V_2O_5 \cdot 0.3H_2O$ film exhibits the best Li^+ intercalation performance, with an initial capacity of 275 mAh/g and a stabilized capacity of 185 mAh/g under a high current density of 100 $\mu A/cm^2$ after 50 cycles. Under a low current density of 10 $\mu A/cm^2$, the capacity of this film can reach 390 mAh/g. Such an enhanced electrochemical property by thermal treatment is ascribed to the reduced water content, the retained interlayer spacing, and the dominant amorphous phase in the film.

Introduction

Vanadium pentoxide (V_2O_5) is a typical intercalation compound, due to its semiconductivity and layered structure.[1,2] A large variety of atomic and molecular species and even polymers can be reversibly intercalated between the layers of V_2O_5 from an electrolyte.[3,4] Accordingly, V_2O_5 has attracted intensive research for many decades to investigate its structure, properties, and techonological applications such as secondary lithium batteries,[5,6] electrochemical supercapacitors,[7,8] and electrochromic displays.[9−11] The strong interest in V_2O_5 originates partially from the high energy density offered by this material. For instance, the intercalation capacity of V_2O_5 films exceeds 15 mC/cm^2, allowing the use of V_2O_5 films as counter electrodes in electrochromic devices with WO_3 active coloring electrodes.[12] The hydrated form of vanadium pentoxide ($V_2O_5 \cdot nH_2O$) has an even higher intercalation capacity than its crystalline analogue. For example, $V_2O_5 \cdot nH_2O$ xerogel film can intercalate up to 3 equiv of lithium ions,[13] while orthorhombic V_2O_5 can only intercalate up to 1 equiv of Li^+ without irreversible alterations of the lattice.[14]

$V_2O_5 \cdot nH_2O$ xerogels are composed of ribbonlike particles and display lamellar ordering, with water molecules intercalated between the layers.[15] These water molecules expand the distance between the layers, and the intercalation capacities of $V_2O_5 \cdot nH_2O$ xerogels are enhanced as a result.[15] Another attractive feature of $V_2O_5 \cdot nH_2O$ is that it can be easily produced from sol−gel synthetic routes at room temperature. There are mainly three convenient sol−gel synthetic routes: (1) acidification of $NaVO_3$ using an ion-exchange process and polymerization of the resultant HVO_3 in water,[16,17] (2) hydrolysis and condensation of vanadium alkoxide,[18,19] and (3) reaction between H_2O_2 and V_2O_5 powder.[20,21] Synthesis of V_2O_5 has been dominated by the $NaVO_3$ route, and detailed research has been done on both the $NaVO_3$ route and the vanadium alkoxide route to investigate the reaction mechanisms. For example, Holland et al. have recently compared thermal behavior and Li^+ diffusion coefficients in $V_2O_5 \cdot nH_2O$ xerogels prepared from the $NaVO_3$ and vanadium alkoxide routes.[22] Their report revealed that the $V_2O_5 \cdot nH_2O$ xerogels made from these two methods have significant differences besides many similarities. Although the $NaVO_3$ route is the most commonly used and the vanadium alkoxide route has been used increasingly, these two methods suffer from a few disadvantages. The $NaVO_3$ route may introduce contamination from sodium ions, and the concentration of vanadium is subject to change due to the additional water in the resin during the ion-exchange process. The ion-exchange process also causes a difficulty for large-scale production. In the vanadium alkoxide route, the high reactivity of the alkoxide and its dependence on pH, temperature, and reactant concentrations make the chemical synthesis of $V_2O_5 \cdot nH_2O$ gels rather delicate and difficult. A complexing agent such as acetic acid or acetyl acetone can be added to control the reaction rate; however these agents also introduce complicated chemistry, and the resultant sol may undergo slow side reactions for a long time. Therefore, the simple and clean $H_2O_2-V_2O_5$ route has attracted more and more attention recently. This method excludes the presence of foreign ions or organic ligands and offers precise control of the vanadium concentration. The synthetic pathway and gelation process of the $H_2O_2-V_2O_5$ route have been studied by ^{51}V NMR and laser Raman spectroscopic techniques recently.[21] Our group has specifically used this method to obtain a stable $V_2O_5 \cdot nH_2O$ sol that can be used in various deposition processes including electrophoretic deposition. We have prepared various forms of orthorhombic V_2O_5 and amorphous $V_2O_5 \cdot nH_2O$ from such a sol, including single-crystal V_2O_5 nanorod arrays,[23,24] $Ni-V_2O_5 \cdot nH_2O$ core−shell nanocable arrays,[25] and $Ag-Ag_xV_2O_5 \cdot nH_2O$ composite films,[26] which demonstrated excellent electrochemical and electrochromic properties. However, $V_2O_5 \cdot nH_2O$ xerogels may suffer from poor cycling life, possibly due to the reaction between lithium and water in $V_2O_5 \cdot nH_2O$ to form Li_2O.[27,28] It has been found that $V_2O_5 \cdot nH_2O$ exhibited a large capacity and good cycling performance when the water content in $V_2O_5 \cdot nH_2O$ was reduced

* Author to whom correspondence should be addressed. Fax: 206-543-3100. E-mail: gzcao@u.washington.edu.

10.1021/jp051275+ CCC: $30.25
Published on Web 05/17/2005

by thermal treatment, and the influence of heating treatment on $V_2O_5 \cdot nH_2O$ has been studied based on $V_2O_5 \cdot nH_2O$ synthesized from the $NaVO_3$ route.[29−32] The purpose of this report is to investigate the thermal behavior and the electrochemical performance of $V_2O_5 \cdot nH_2O$ film synthesized from the $H_2O_2-V_2O_5$ route. We aim to prepare $V_2O_5 \cdot nH_2O$ films with various water contents and investigate their capacities and cycling performance. X-ray diffraction (XRD), electrochemical measurements, and scanning electron microscopy (SEM) were used to study the structure and properties of these films.

Experimental Section

A diluted $V_2O_5 \cdot nH_2O$ sol was prepared using a method reported by Fontenot et al. [21] with V_2O_5 (Alfa Aesar) and 30% H_2O_2 (J. T. Baker) as precursors. V_2O_5 powder was dissolved in a H_2O_2 solution with a V_2O_5 concentration of 0.15 M. The resulting solution has a H_2O_2/V_2O_5 ratio of 8:1. After being stirred for 1.5 h at room temperature, the excess H_2O_2 was decomposed by sonication, and a yellow-brown gel was obtained. The resultant gel was then redispersed in deionized water, resulting in the formation of a brownish sol, which contained 0.01 mol/L vanadium with a pH of 2.7. The primary vanadium species in the colloidal dispersion are nanoparticles of hydrated vanadium oxide. $V_2O_5 \cdot nH_2O$ films were prepared by spreading 65 μL of $V_2O_5 \cdot nH_2O$ sol onto indium titanium oxide (ITO) substrates. The samples were then dried under ambient conditions and annealed at various temperatures (110, 250, 300, and 330 °C) in air for 5 h. All the samples have a geometric area of ~0.5 cm^2. All the samples were stored in a desiccator before measurements.

To obtain $V_2O_5 \cdot nH_2O$ xerogels for thermal gravimetric analysis (TGA) measurements, a more concentrated $V_2O_5 \cdot nH_2O$ sol was synthesized as follows. Approximately 0.136 g of V_2O_5 powder was dissolved in 2 mL of deionized H_2O and 0.603 mL of H_2O_2 solution. The suspension was stirred until the V_2O_5 powder totally dissolved, resulting in a clear and dark red solution. The solution was then sonicated to obtain a yellow-brown gel that was dispersed into deionized H_2O in a molar concentration of 0.025 M. The sol was dried under ambient conditions. The measurement was performed on a thermal gravimetric analyzer (Perkin-Elmer TGA7) with a temperature range from room temperature to 500 °C in a N_2 atmosphere at a heating rate of 5 °C/min. Scanning electron microscopy (JEOL JSM-5200) was used to characterize the morphology of $V_2O_5 \cdot nH_2O$ films before and after electrochemical redox cycles. XRD patterns of the $V_2O_5 \cdot nH_2O$ films were obtained by using a Philips PW1820 diffractometer. Electrochemical properties of the $V_2O_5 \cdot nH_2O$ film electrode were investigated using a standard three-electrode cell, with the 1 M $LiClO_4$ solution in propylene carbonate as the electrolyte, a Pt mesh as the counter electrode, and $Ag/AgNO_3$ as the reference electrode. Cyclic voltammetric (CV) and chronopotentiometric measurements of these films were carried out by using an electrochemical analyzer (CH Instruments, Model 605B).

Results and Discussion

Figure 1 presents a top view and a cross-sectional SEM image, showing the coherent and homogeneous $V_2O_5 \cdot nH_2O$ film that was annealed at 250 °C. In general, $V_2O_5 \cdot nH_2O$ films show smooth and featureless surface morphology; no detectable cracks or pinholes were observed, and the thickness of the film is ~1 μm. There is no appreciable difference in surface morphology or thickness for films obtained at room temperature or annealed at a temperature ≤250 °C.

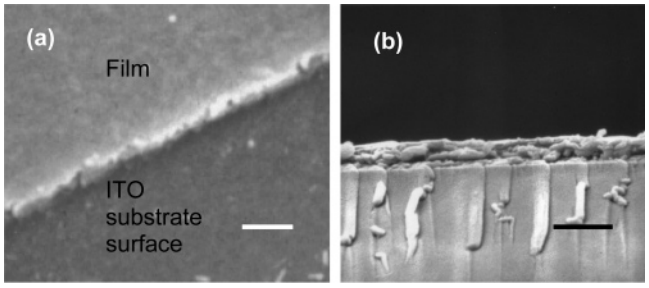

Figure 1. SEM images of (a) a top view of the $V_2O_5 \cdot 0.3H_2O$ film with part of the film scratched off (scale bar = 2 μm) and (b) a cross section of the $V_2O_5 \cdot 0.3H_2O$ film annealed at 250 °C (scale bar = 2 μm).

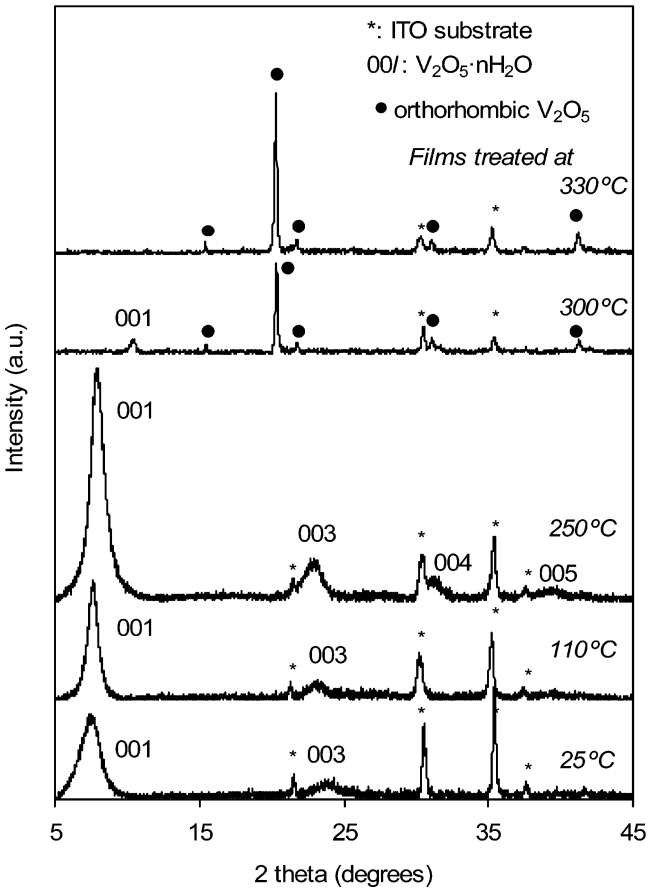

Figure 2. XRD patterns of $V_2O_5 \cdot nH_2O$ films treated at 25, 110, 250, 300, and 330 °C.

Figure 2 presents XRD patterns of samples treated at 25, 110, 250, 300, and 330 °C, indicating structural changes from almost amorphous to orthorhombic V_2O_5. The spectra of films treated at 25, 110, and 250°C have broad peaks, indicative of an amorphous nature and similar to those of $V_2O_5 \cdot nH_2O$ xerogels reported in the literature.[15] The most intense peak is (001) diffraction, which is related to the ribbon stacking along the *c*-axis. Thus, the intensity of the (001) peak is assumed to be proportional to the fraction of quasi-ordered crystalline material in the samples. It can be seen in Figure 2 that the (001) peak intensity gradually increases as the annealing temperature is increased and other weak peaks such as (003) and (004) are more distinct for the sample treated at 250 °C, suggesting a gradual increase in the portion of quasi-ordered region in the films. Thermal treatments at even higher temperatures lead to modified materials progressively turning into crystalline V_2O_5. The film treated at 300 °C shows XRD patterns for both $V_2O_5 \cdot$

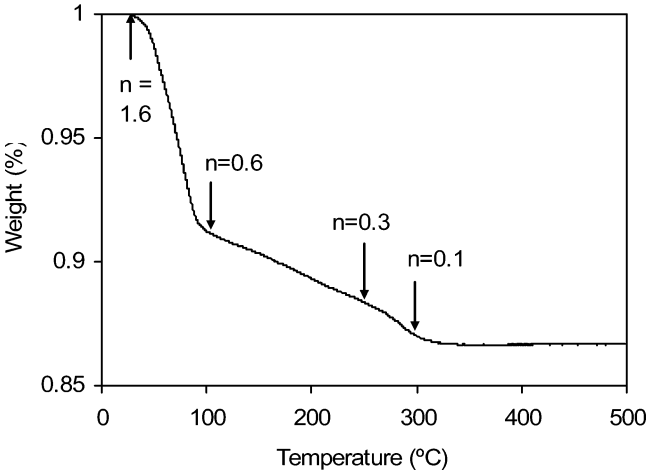

Figure 3. TGA curve for $V_2O_5 \cdot nH_2O$ xerogels.

nH_2O and orthorhombic V_2O_5, while the film treated at 330 °C shows pure orthorhombic V_2O_5, indicating transformation is complete at this temperature.

Figure 3 shows a thermogravimetric trace for $V_2O_5 \cdot nH_2O$ xerogels. It reveals the existence of 1.6 mol of water per mole of oxide at room temperature (assuming V_2O_5 as the solid phase after heating at >330 °C, whereas water is the only volatile phase in the initial film). This result and the shape of the TGA curve are similar to those of xerogels prepared by $NaVO_3$ and alkoxide routes.[22] The weight change profile for the xerogel is characterized by a steep loss between room temperature and 100 °C, followed by a more gradual weight loss up until 330 °C. Thermal treatment at 110 °C produced a xerogel with the $V_2O_5 \cdot 0.6H_2O$ composition. Continued heating to 250 °C produced $V_2O_5 \cdot 0.3H_2O$ by removing bound water. Heating above 300 °C induced the loss of tightly bound water and crystallization of the material, as discussed in the XRD results. The TGA profile for loss of the weakly bound and bound water from $V_2O_5 \cdot nH_2O$ is slightly different from those prepared from the $NaVO_3$ and vanadium alkoxide routes.[21]

For $V_2O_5 \cdot nH_2O$, the interlayer spacing d can be calculated from the diffraction angle of the (001) peak, and the grain size can be obtained from its full width at half-maximum (FWHM) using Scherrer's forumla.[33,34] Figures 4a and 4b summarize the dependencies of interlayer spacing and grain size on the n value in $V_2O_5 \cdot nH_2O$, respectively. For samples treated at 25, 110, and 250 °C, the interlayer spacings show a slight decrease from 11.74 to 11.15 Å as the temperature increases; however the change is rather small, and the results are consistent with the value of 11.5 Å reported in the literature.[15] For the sample annealed at 300 °C in which low-crystalline $V_2O_5 \cdot nH_2O$ coexists with orthorhombic V_2O_5, the interlayer spacing of $V_2O_5 \cdot nH_2O$ is 8.43 Å, apparently smaller than the samples treated from 25 to 250 °C. The trend in the change of the grain size is consistent with that in the change of the interlayer spacing. The grain sizes for $V_2O_5 \cdot nH_2O$ between 25 and 250 °C are rather similar and are in a range of 4.8−8.5 nm, while the grain size for $V_2O_5 \cdot nH_2O$ at 300 °C is increased considerably to 21.2 nm. These results explain why $V_2O_5 \cdot nH_2O$ films annealed at different temperatures ≤250 °C have similar morphologies and thicknesses as mentioned earlier, since these films have similar grain sizes and interlayer spacings. TGA results have shown that 110 °C corresponds to $V_2O_5 \cdot 0.6H_2O$ and 250 °C to $V_2O_5 \cdot 0.3H_2O$. It can be concluded that interlayer spacing and grain size do not alter much when only bound water (reversibly absorbed or hydrogen-bonded water) is removed. These parameters will alter considerably only when tightly bound (chemically bonded) water is removed and the material is on the verge of crystallization.

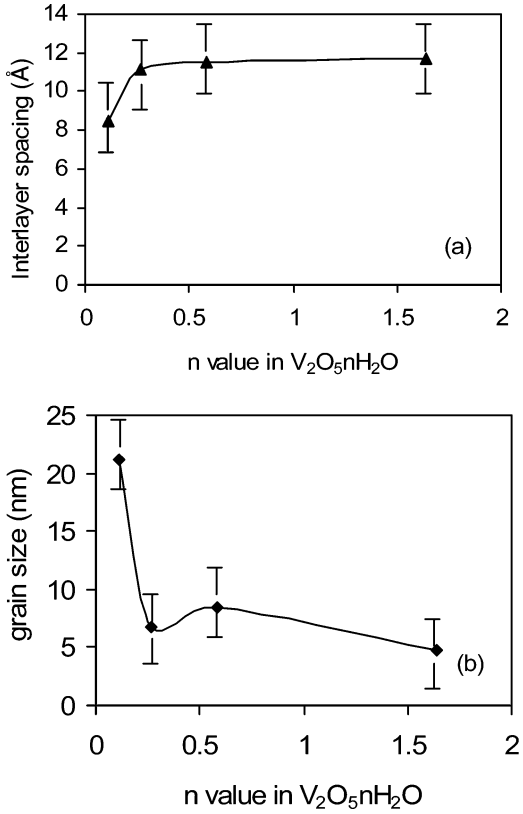

Figure 4. (a) Dependence of interlayer spacing on the n value in $V_2O_5 \cdot nH_2O$. (b) Dependence of grain size on the n value in $V_2O_5 \cdot nH_2O$.

Figure 5a compares the first CV cycle of the films treated at different temperatures using a scan rate of 10 mV/sec. The cyclic voltammogram of $V_2O_5 \cdot nH_2O$ film obtained at 25 °C has cathodic peaks at −1.1 and −0.75 V, which correspond to Li^+ intercalation, and anodic oxidation peaks at −0.83 and at −0.41 V, which are attributed to Li^+ extraction. The $V_2O_5 \cdot nH_2O$ films obtained at 110 and 250 °C exhibit similar electrochemical behaviors to that of a $V_2O_5 \cdot nH_2O$ film treated at room temperature, showing broad charge/discharge peaks characteristic of the low-crystalline nature of the $V_2O_5 \cdot nH_2O$ films. The cyclic voltammogram of the crystalline V_2O_5 film obtained at 300 °C has cathodic peaks at −0.49 and −0.33 V, and anodic oxidation peaks at −0.35 and −0.03 V. These peaks are more distinct than those of $V_2O_5 \cdot nH_2O$ films. Figures 5b−d show the first and the tenth CV cycles for the $V_2O_5 \cdot nH_2O$ films obtained at 25, 110, and 250 °C. Repetitive cycling between 0.4 and −1.6 V vs Ag/Ag^+ did not alter the current response of the films significantly, suggesting good electrochemical stability of the $V_2O_5 \cdot nH_2O$ films.

Although the Li^+ extraction/intercalation behaviors were found to be similar in the $V_2O_5 \cdot nH_2O$ films with $n = 1.6$, 0.6, and 0.3, the discharge capacities of these $V_2O_5 \cdot nH_2O$ films are different with the annealing temperature. Figure 6a compares the chronopotentiometric (CP) curves of $V_2O_5 \cdot nH_2O$ films treated at 25, 110, 250, and 300 °C. All the films were discharged to −1.6 V vs Ag/Ag^+ at a high current density of 100 $\mu A/cm^2$. The initial discharge starts at a lower potential than the following discharges (0.4 V), due to spontaneous reduction of the $V_2O_5 \cdot nH_2O$ xerogel, which has been reported in the literature.[30] The curve for the sample obtained at 25 °C has a continuously sloping shape that is characteristic of low-

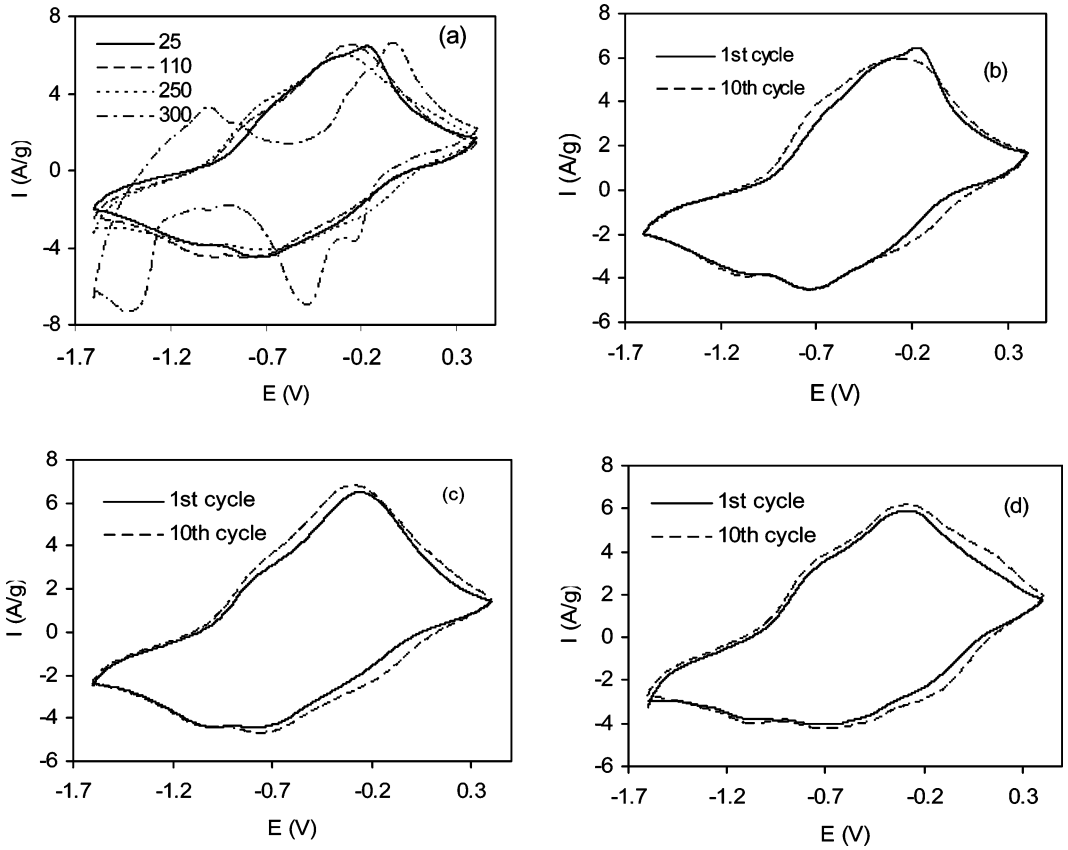

Figure 5. (a) CV cycles of the $V_2O_5 \cdot nH_2O$ films treated at 25, 110, 250, and 300 °C. The first and tenth CV cycles of the $V_2O_5 \cdot nH_2O$ film treated at (b) 25, (c) 110, and (d) 250 °C, respectively. The scan rate was 10 mV/s.

crystalline structure, while those for the thermally annealed films develop a more stepwise shape, resulting from the further crystallization in these samples. The curve for the film annealed at 300 °C has a distinctly different shape than others, due to the existence of the orthorhombic phase. The discharge capacities for the films obtained at 25, 110, 250, and 300 °C are 150, 185, 275, and 250 mAh/g, respectively. Figure 6b summarizes the Li^+ intercalation capacity as a function of current density for $V_2O_5 \cdot nH_2O$ films. At all current densities, the capacity increases with annealing temperature for temperature ≤250 °C and decreases afterward. At a low current density of 10 μA/cm^2, the film annealed at 250 °C delivers a high capacity of 390 mAh/g, intercalating 2.6 equiv of Li^+. When such low current density is applied, the capacities of all four films are closer since the intercalation process proceeds to thermodynamic equilibrium. However, at a higher current density such as 20 μA/cm^2, the film treated at 250 °C achieves 1.3 times the capacity of the film treated at 300 °C, 1.7 times the capacity of the film treated at 110 °C, and 2.2 times the capacity of the film treated at 25 °C.

Figure 7a shows the CP curves of the $V_2O_5 \cdot 0.3H_2O$ film (annealed at 250 °C) measured at the 1st, 21st, and 50th discharge in the range between 0.4 and −1.6 V vs Ag/Ag^+ and under the current density of 100 μA/cm^2. The initial irreversible discharge capacity is found to be 260 mAh/g, which is larger than the 21st reversible discharge capacity of 190 mAh/g. The 50th discharge curve is almost identical to the 21st curve and suggests the good cyclicality of the film after 20 cycles. Figure 7b presents the last 10 discharge/charge curves among the 50 redox cycles (i.e., from the 41st to the 50th discharge/charge curves) of the $V_2O_5 \cdot 0.3H_2O$ film. The film was cycled 50 times in the range between 0.4 and −1.6 V vs Ag/Ag^+ at a current density of 100 μA/cm^2. It can be seen that these cycles present almost identical capacities, indicating that the $V_2O_5 \cdot 0.3H_2O$ film electrode is able to retain a stabilized capacity of 185 mAh/g and demonstrates good reversibility. Figure 8 summarizes and compares cycling performances of the $V_2O_5 \cdot nH_2O$ films treated at 25, 110, 250, and 300 °C at the high current density of 100 μA/cm^2. It can be seen that the capacities of all three films degrade initially then become more or less stabilized. The film obtained at 25 °C has the lowest capacity and the least-satisfying cycling performance among the three xerogel films. The film annealed at 300 °C has a high initial capacity; however it shows the most drastic electrochemical degradation, possibly due to the crystalline phase. The film annealed at 250 °C delivers the highest initial capacity and retains a stable capacity of 185 mAh/g after 20 cycles.

SEM has been used to examine the possible change of surface morphologies of the films. Figures 9a and 9b show the surfaces of the $V_2O_5 \cdot 0.3H_2O$ film before and after 50 redox cycles, respectively; the $V_2O_5 \cdot 0.3H_2O$ was annealed at 250 °C and demonstrated the best electrochemical performance as discussed earlier in this paper. It can be seen that after electrochemical cycles the surface of the film becomes much rougher and there are small cracks due to expansion/contraction during the Li^+ intercalation/extraction process. However, the film remains in good condition, and no severe disruption or delamination has been detected, which explains its good cyclicality. The small cracks most likely occurred during initial cycles and cause the degradation of capacity within the first 20 cycles as shown in Figure 8. Such structural defects allow more volume changes for further cycling and in part results in the sustainable electrochemical performance after 20 cycles. In addition, XRD analysis has shown $V_2O_5 \cdot 0.3H_2O$ obtained at 250 °C keeps the large interlayer spacing and the amorphous phase. The volume changes of amorphous electrode during cycling are more

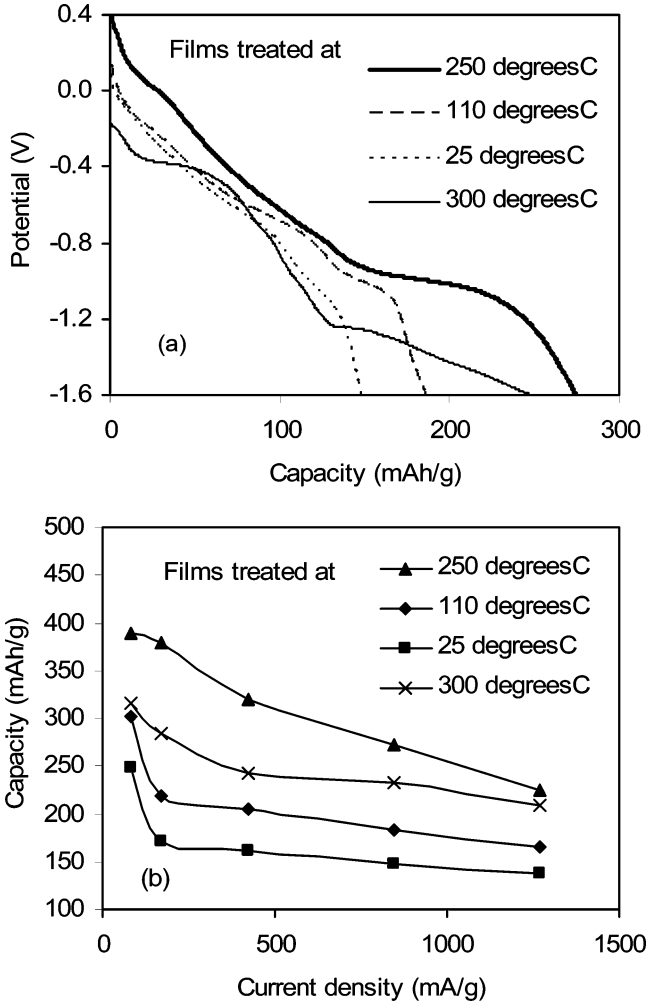

Figure 6. (a) Discharge curves of $V_2O_5 \cdot nH_2O$ films obtained at 25, 110, 250, and 300 °C under a current density of 100 μA/cm^2 (850 mA/g). (b) Relationship between discharge capacity and current density for $V_2O_5 \cdot nH_2O$ films treated at 25, 110, 250, and 300 °C. The voltage ranges from 0.4 to −1.6 V vs Ag/Ag$^+$.

uniform than those in the crystalline one. The apparent volume of the $V_2O_5 \cdot 0.3H_2O$ film can be computed to be 5.0×10^{-5} cm^3 from the geometric area (0.5 cm^2) and the thickness (1 μm from the cross-sectional SEM image (Figure 1b)). Therefore, the density of the film is calculated to be 1.5 g/cm^3, which is much lower than the reported density of $V_2O_5 \cdot nH_2O$ (2.87 g/cm^3).[35] The porosity of the film is estimated to be ~40%. The small water content, 0.3 mol of water per mole of V_2O_5 in this film, may explain its good cycling performance as well, since water in $V_2O_5 \cdot nH_2O$ can react with lithium to limit the performance.

Conclusions

$V_2O_5 \cdot nH_2O$ films have been prepared from the sol−gel $H_2O_2-V_2O_5$ route. The films annealed at different temperatures have been demonstrated to behave very differently as host materials for Li$^+$ intercalation. TGA measurements, XRD, electrochemical methods, and SEM have been employed to reveal the structure and properties of these films. Treatment at 25, 110, and 250 °C produced xerogels with compositions of $V_2O_5 \cdot 1.6H_2O$, $V_2O_5 \cdot 0.6H_2O$, and $V_2O_5 \cdot 0.3H_2O$, respectively. XRD analysis indicates the basal spacing of these three xerogels is rather similar and treatment ≤250 °C does not change the interlayer distance of $V_2O_5 \cdot nH_2O$ significantly. Electrochemical

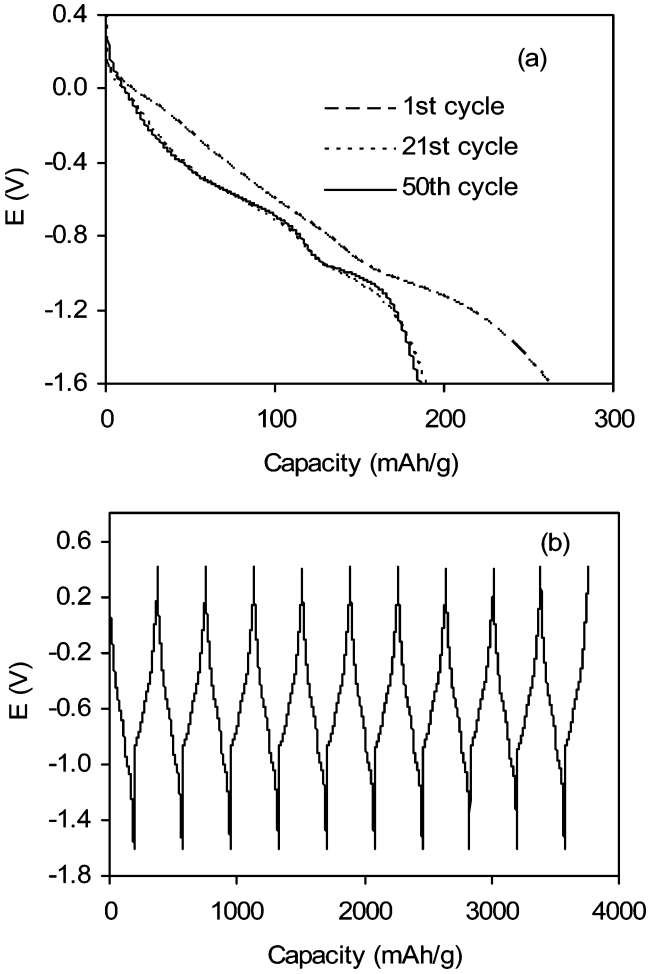

Figure 7. Discharge behavior of a $V_2O_5 \cdot 0.3H_2O$ film obtained at 250 °C under a current density of 100 μA/cm^2: (a) the discharge curves of the 1st, 21st, and 50th cycles and (b) the 41st to the 50th cycles. The voltage ranges from 0.4 to −1.6 V vs Ag/Ag$^+$.

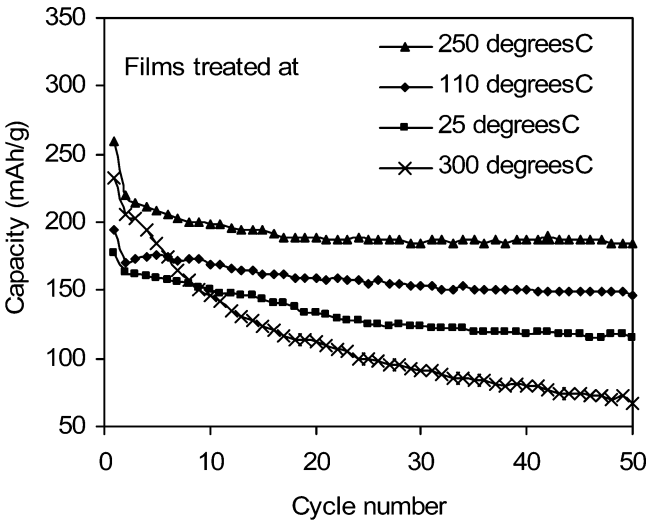

Figure 8. Cycling performance at a current density of 100 μA/cm^2 for $V_2O_5 \cdot nH_2O$ films obtained at 25, 110, 250, and 300 °C. The voltage ranges from 0.4 to −1.6 V vs Ag/Ag$^+$.

characterizations demonstrate that the $V_2O_5 \cdot 1.6H_2O$ film has the lowest capacity and the least-satisfying cycling performance, while the $V_2O_5 \cdot 0.3H_2O$ film exhibits the best performance, with an initial capacity of 275 mAh/g and a stabilized capacity of 185 mAh/g under a high current density of 100 μA/cm^2. Under a low current density of 10 μA/cm^2, the capacity of this film

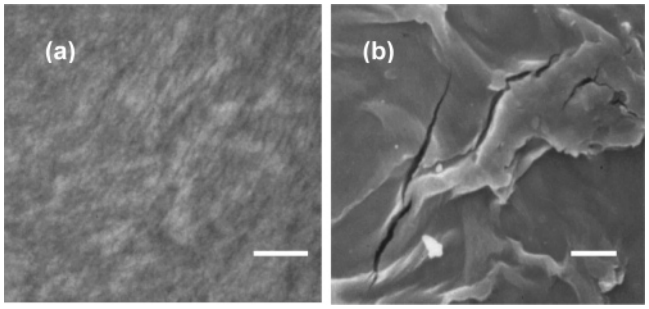

Figure 9. SEM images of $V_2O_5 \cdot 0.3H_2O$ film (obtained at 250 °C) (a) before electrochemical cycling (scale bar = 1 μm) and (b) after electrochemical cycling (scale bar = 5 μm).

can reach 390 mAh/g. The reason is discussed as follows. Removing too little water limits the electrochemical performance because a significant amount of water may react with lithium to form Li_2O. Removal of too much water deteriorates the intercalation performance as well, due to the shrinkage of the interlayer distance and the emergence of the crystalline phase. $V_2O_5 \cdot 0.3H_2O$ obtained at 250 °C was found to be an optimal composition, which has the least possible water amount and keeps the large interlayer distance and the amorphous phase.

Acknowledgment. Y.W. acknowledges the financial support from the Ford Motor Company fellowship. H.M.S. acknowledges the graduate fellowship from the Joint Institute of Nanoscience and Nanotechnology, University of Washington and Pacific Northwest National Laboratories. T.C. acknowledges the Intel Company fellowship. The authors thank Professor Brian D. Flinn for his help in using the thermal gravimetric analyzer.

References and Notes

(1) Bachmann, H. G.; Ahmend, F. R.; Barnes, W. H. *Z. Kristallorgr.* **1961**, *115*, 110.

(2) Whittinham, M. S. *J. Electrochem. Soc.* **1976**, *123*, 315.

(3) Kanatzidis, M. G.; Wu, C. G.; Marcy, H. O.; DeGroot, D. C.; Kannewurf, C. R. *Chem. Mater.* **1990**, *2*, 222.

(4) Wu, C. G.; DeGroot, D. C.; Marcy, H. O.; Schindler, J.; Kannewurf, C. R.; Liu, Y. J.; Hirpo, W.; Kanatzidis, M. G. *Chem. Mater.* **1996**, *8*, 1992.

(5) Park, H. K.; Smryl, W. H.; Ward, M. D. *J. Electrochem. Soc.* **1995**, *142*, 15.

(6) Swider-Lyons, K. E.; Love, C. T.; Rolison, D. R. *Solid State Ionics* **2002**, *152*−*153*, 99.

(7) Shimizu, A.; Tsumura, T.; Inagaki, M. *Solid State Ionics* **1993**, *63*−*65*, 479.

(8) Portion, E.; Salle, A. L. G. A.; Verbaere, A.; Piffard, Y.; Guyomard, D. *Electrochim. Acta* **1999**, *45*, 197.

(9) Granqvist, C. G. *Handbook of Inorganic Electrochromic Materials*; Elsevier: Amsterdam, 1995.

(10) Cogan, S. F. In *Large Area Chromogenics: Materials and Devices for Transmittance Control*; Lampert, C. M., Granqvist, C. G., Eds.; SPIE Institutes for Advanced Optical Technologies IS04; SPIE Press: Bellingham, WA, 1990; p 313.

(11) Özer, N. *Thin Solid Films* **1997**, *305*, 80.

(12) Cogan, S. F.; Nguyen N. M.; Perrotti, S. J.; Rauh, R. D. *J. Appl. Phys.* **1989**, *66*, 1333.

(13) Livage, J. *Chem. Mater.* **1991**, *3*, 578.

(14) Winter, M.; Besenhard, J. O.; Spahr, M. E.; Novak, P. *Adv. Mater.* **1998**, *10*, 725.

(15) Petkov, V.; Trikalitis, P. N.; Bozin, E. S.; Billinge, S. J. L.; Vogt T.; Kanatzidis, M. G. *J. Am. Chem. Soc.* **2002**, *124*, 10157.

(16) Livage, J. *Coord. Chem. Rev.* **1998**, *178*−*180*, 999.

(17) Le, D. B.; Passerini, S.; Tipton, A. L.; Owens, B. B.; Smyrl, W. H. *J. Electrochem. Soc.* **1995**, *142*, L102.

(18) Harreld, J. H.; Dunn, B.; Nazar, L. F. *Int. J. Inorg. Mater.* **1999**, *1*, 135.

(19) Desai, S. D.; Cussler, E. L. *Langmuir* **1998**, *14*, 277.

(20) Alnoso, B.; Livage, J. *J. Solid State Chem.* **1999**, *148*, 16.

(21) Fontenot, C. J.; Wiench, J. W.; Pruski, M.; Schrader, G. L. *J. Phys. Chem. B* **2000**, *104*, 11622.

(22) Hollad, G. P.; Huguenin, F.; Torresi, R. M.; Buttry, D. A. *J. Electrochem. Soc.* **2003**, *150*, A721.

(23) Takahashi, K.; Limmer, S. J.; Wang, Y.; Cao, G. Z. *Jpn. J. Appl. Phys.* **2005**, *44*, 662.

(24) Takahashi, K.; Wang, Y.; Cao, G. Z. *Appl. Phys. Lett.* **2005**, *86*, 053102.

(25) Takahashi, K.; Wang, Y.; Cao, G. Z. *J. Phys. Chem. B* **2005**, *109*, 48.

(26) Wang, Y.; Lee, K.; Shang, H.; Wiley, B.; Xia, Y.; Cao, G. Z. *Phys. Status Solidi A* **2005**, *202*, R79.

(27) Linden, D. In *Handbook of Batteries*, 2nd ed.; McGraw-Hill: New York, 1995.

(28) Almeida, E. C.; Abbate, M.; Rosolen, J. M. *Solid State Ionics* **2001**, *140*, 241.

(29) Wang, J.; Curtis, C. J.; Schulz, D. L.; Zhang, J. *J. Electrochem. Soc.* **2004**, *151*, A1.

(30) West, K.; Zachau-Christinansen, B.; Jacobeen, T. *J. Power Sources* **1993**, *43*−*44*, 127.

(31) Cuentas-Gallegos, A. K.; Gómez-Romero, P. In *New Trends in Intercalation Compounds for Energy Storage*; Julien, C., Pereira-Ramos, J. P., Momchilov, A., Eds.; NATO Science Series II: Mathematics, Physics and Chemistry 61; Kluwer Academic Publishers: New York, 2002; p 535.

(32) Brunello, C. A.; Graeff, C. F. O. *J. Non-Cryst. Solids* **2002**, *304*, 265.

(33) Cao, G. Z. *Nanostructures and Nanomaterials, Synthesis, Properties and Applications*; Imperial College Press: London, 2004.

(34) Birks, L. S.; Friedman, H. *J. Appl. Phys.* **1946**, *17*, 687.

(35) Liu, Y. J.; Cowen, J. A.; Kaplan, T. A.; DeGroot, D. C.; Schindler, J.; Kannewurf, C. R.; Kanatzidis, M. G. *Chem. Mater.* **1995**, *7*, 1616.